Materials
Horizons

ROYAL SOCIETY
OF CHEMISTRY

COMMUNICATION

View Article Online
View Journal | View Issue

Check for updates

Cite this: *Mater. Horiz.*, 2023, **10**, 4389

Received 11th May 2023,
Accepted 10th July 2023

DOI: 10.1039/d3mh00716b

rsc.li/materials-horizons

Anion-induced robust ferroelectricity in sulfurized pseudo-rhombohedral epitaxial $BiFeO_3$ thin films *via* polarization rotation†

Guoqiang Xi,[a] Zhao Pan,*[b] Yue-Wen Fang,*[cd] Jie Tu,[a] Hangren Li,[a] Qianqian Yang,[a] Chen Liu,[e] Huajie Luo,[f] Jiaqi Ding,[g] Shuai Xu,[b] Shiqing Deng,[f] Qingxiao Wang,[h] Dongxing Zheng,[e] Youwen Long,[bi] Kuijuan Jin,[b] Xixiang Zhang,[e] Jianjun Tian[a] and Linxing Zhang*[a]

Polarization rotation caused by various strains, such as substrate and/or chemical strain, is essential to control the electronic structure and properties of ferroelectric materials. This study proposes anion-induced polarization rotation with chemical strain, which effectively improves ferroelectricity. A method for the sulfurization of $BiFeO_3$ thin films by introducing sulfur anions is presented. The sulfurized films exhibited substantial enhancement in room-temperature ferroelectric polarization through polarization rotation and distortion, with a 170% increase in the remnant polarization from 58 to 100.7 μC cm^{-2}. According to first-principles calculations and the results of X-ray absorption spectroscopy and high-angle annular dark-field scanning transmission electron microscopy, this enhancement arose from the introduction of S atoms driving the redistribution of the lone-pair electrons of Bi, resulting in the rotation of the polarization state from the [001] direction to the [110] or [111] one. The presented method of anion-driven polarization rotation might enable the improvement of the properties of oxide materials.

New concepts

$BiFeO_3$ (BFO), a perovskite-type material, has been extensively studied due to its high Curie temperature and large spontaneous polarization. While much attention has been given to modifying the ferroelectric properties of BFO thin films by replacing A-site (Bi) and/or B-site (Fe) cations, the effect of anion-site substitution remains unexplored. Thus, a feasible anion-induced strain engineering was proposed. The polarization state was tuned by anion-induced strain for achieving enhanced polarization, which has been supported by density functional theory calculations and a comprehensive set of measurements. The anion-driven polarization rotation presents enormous potential in other perovskite-type oxide materials, paving the way for a new generation of multifunctional materials with exceptional performance.

Introduction

Tuning the polarization state is crucial for modifying the ferroelectric and piezoelectric properties of ferroelectric thin films. In particular, regulating the polarization direction is important for achieving tunable polarization values, energy storage, and piezoelectric response.[1,2] For instance, polarization rotation can enhance the piezoelectric properties of $PbTiO_3$, $K_{1-x}Na_xNbO_3$, $BiFeO_3$ (BFO), and other systems.[3–6] The fast polarization rotation induced by the low energy barrier of polar nanoregions significantly contributes to the decent energy storage properties of $NaNbO_3$-based ceramics.[7] BFO, a lead-free multifunctional perovskite-type (ABO_3) ferroelectric material with large polarization, has seen unexpected advances in its synthesis, structure, ferromagnetic, and ferroelectric properties.[8–12] The ferroelectricity of bulk BFO is a consequence of the presence of lone pair electrons on Bi^{3+} cations, which create local dipole moments due to the asymmetric electronic charge distribution around the Bi sites.[13,14] Thus, the controlled rotation or distortion of the local dipole in BFO thin films may induce their polarization mutation, allowing for new states of matter and phenomena.

A prominent example is the biaxial strain from the substrate,[15,16] which is based on lattice mismatch to apply epitaxial biaxial strain on films and has been successfully used

---

[a] *Institute for Advanced Materials Technology, University of Science and Technology Beijing, Beijing 100083, China. E-mail: linxingzhang@ustb.edu.cn*
[b] *Beijing National Laboratory for Condensed Matter Physics, Institute of Physics, Chinese Academy of Sciences, Beijing 100190, China. E-mail: zhaopan@iphy.ac.cn*
[c] *Centro de Física de Materiales (CSIC-UPV/EHU), Manuel de Lardizabal pasealekua 5, 20018 Donostia/San Sebastián, Spain. E-mail: fyuewen@gmail.com*
[d] *Fisika Aplikatua Saila, Gipuzkoako Ingeniaritza Eskola, University of the Basque Country (UPV/EHU), Europa Plaza 1, 20018 Donostia/San Sebastián, Spain*
[e] *Physical Science and Engineering Division, King Abdullah University of Science and Technology (KAUST), Thuwal 23955-6900, Saudi Arabia*
[f] *Beijing Advanced Innovation Center for Materials Genome Engineering, Department of Physical Chemistry, University of Science and Technology Beijing, Beijing 100083, China*
[g] *Key Laboratory for Micro/Nano Optoelectronic Devices of Ministry of Education, School of Physics and Electronics, Hunan University, Changsha 410082, China*
[h] *Corelab, King Abdullah University of Science and Technology (KAUST), Thuwal 23955-6900, Saudi Arabia*
[i] *Songshan Lake Materials Laboratory, Dongguan, Guangdong 523808, China*

† Electronic supplementary information (ESI) available. See DOI: **https://doi.org/10.1039/d3mh00716b**

to deform or distort the lattice for novel features. For example, single-phase BFO thin films have been epitaxially grown on single crystal $SrTiO_3$ (STO) (100) by pulsed laser deposition,[17] which exhibits a tetragonal-like (T′) phase (space group *P*4*mm*) structure with an axial ratio (*c*/*a*) of 1.016 and a small monoclinic distortion of $\sim 0.5^\circ$ owing to substrate compressive stress. This also inspired others to prepare epitaxial BFO thin films onto $LaAlO_3$ (LAO) substrates with highly mismatched lattice parameters, possessing a pure T′-phase BFO thin film ($c/a = 1.24$) with a large compressive epitaxial strain of $\sim$4.5%.[18] At the same time, epitaxial films with different orientations can also be realized by different biaxial strains of various substrate orientations, realizing the control of the polarization rotation.[19,20] Another effective route is the chemical strain from composition substitution.[6,21] It turns the crystal symmetry from the rhombohedral phase of pure BFO into another structure. It has been reported that replacing A-sites of BFO thin films with rare earth elements, such as Sm and Gd, can alter their structure from a ferroelectric rhombohedral phase into a paraelectric orthorhombic phase.[22] Moreover, researchers have tried to replace Fe ions with elements having a larger ionic radius, expecting larger *c*/*a* ratio and better performance. For instance, the B-sites of epitaxial BFO thin films have been substituted with cobalt, resulting in structural distortion from M_C-type monoclinic to M_A-type monoclinic, and enhancing the piezoelectric response in the M_C-phase *via* polarization rotation.[23] While much attention has been given to modifying the ferroelectric properties of BFO thin films by replacing A-site (Bi) and/or B-site (Fe) cations, there have been few attempts to substitute the O-sites with other anions.

Studies of the effects of anion substitution in various oxide perovskites on the crystal structure, electrons, and properties are few and far between in the past few decades, compared with cation substitution. The common anions used to replace oxygen have been reported to include mainly F, Cl, C, N, S, *etc.*[24,25] The different valences, electronegativities, and ionic radii of hetero-anions should affect the crystal/electronic structure of BFO thin films. Furthermore, anions hybridize with both A- and B-sites in perovskite oxide, so anion substitution makes it easier to regulate chemical strain. Since sulfur ($3s^23p^4$) has the same number of valence electrons as oxygen ($2s^22p^4$), the substitution of S atoms on the O-sites is conducive to avoiding the introduction of undesirable holes or defects.[26,27] Morever, first-principles calculations have shown that the replacement of O ions by S ones drives the increase of polarization and optical absorption in $PbTiO_3$,[28] $BiCoO_3$,[29] and $KNbO_3$.[27] However, the synthesis of high-quality single-crystal epitaxial films is hindered by the volatility of the S atoms, and the effect of sulfide on the ferroelectric properties in epitaxial films is unclear.

Here, to the best of our knowledge, we investigated for the first time the polarization rotation of anion sulfurization driven in the system of BFO. The high-quality sulfurized BFO epitaxial thin films can be grown *via* a two-step method. Our findings show that the sulfurization significantly enhances the macroscopic ferroelectricity of BFO thin films by 1.74 times, with the remnant polarization P_r increasing from 58.0 $\mu C\ cm^{-2}$ in pristine BFO thin films to a remarkable 100.7 $\mu C\ cm^{-2}$ in sulfurized BFO thin films. The substantial increase in the macroscopic ferroelectric properties has been confirmed by the optical second-harmonic generation (SHG). Moreover, high-energy synchrotron X-ray absorption spectroscopy (XAS), scanning transmission electron microscopy (STEM), high-angle annular dark-field (HAADF) STEM, and Raman spectroscopy measurements revealed polarization rotation and electronic reconstruction induced by sulfurization. The current study indicates sulfurization as a potential method to increase polarity in epitaxial BFO films, which may be also applicable to other perovskite-type oxide materials.

Results and discussion

Because ferroelectricity in BFO is mainly driven by the $6s^2$ lone-pair electrons of Bi^{3+}, we visualized how the lone-pair electrons break the inversion symmetry using the electron localization function (ELF) obtained from first-principles density functional theory (DFT) calculations. The ELF has been widely used to study the ferroelectric and chemical properties of ferroelectrics and polar metals,[30–32] which indicates the degree of localization of the electronic density in a material. It is a real-valued function with values between 0 and 1, where large values indicate a high localization degree. In the DFT calculations, a 40-atom pseudo-cubic BFO model with initial polarization along [001] is considered, which can accommodate various displacement patterns and octahedral rotations. BFO showed G-type antiferromagnetic (G-AFM) ordering below the Néel temperature (640 K); hence, this ordering was used in the DFT calculations. By constraining the space group to *P*4*mm*, according to Wang *et al.*,[17] the polarization of BFO was calculated to be around 60 $\mu C\ cm^{-2}$, which is consistent with the formerly reported values of 50–60 $\mu C\ cm^{-2}$. To simulate a BFOS thin film, we adopted the virtual crystal approximation (VCA) method, which can avoid the need to generate and study large supercells containing many disorder or dopant atoms, because it is precise in addressing the total energy and polarization displacements in ferroelectrics.[33] Further details of our DFT calculations are available in the ESI.† Fig. 1(A) shows the ELF of the BFO and BFOS thin films, where the isovalue was set to 0.92. As expected, in both cases, the ELF is close to 1 because the lone-pair electrons do not participate in the chemical bonding and are highly localized around the Bi atoms. In BFO, the ELF of the lone-pair electrons is primarily on one side of the Bi ions along the [001] direction, causing inversion symmetry breaking and the resulting ferroelectric polarization in that direction. As for ELF of BFOS with [111] polarization, the lone-pair electrons are unevenly distributed by one side of the Bi ions along the [111] direction, which drives the inversion symmetry breaking and the consequent polarization displacements along that direction. This ELF comparison suggests that the introduction of S atoms drives the re-distribution of the lone-pair electrons of Bi and a rotation of the polarization vector, in turn, plays important roles in determining the macroscopic properties of oxide perovskites. Therefore, our

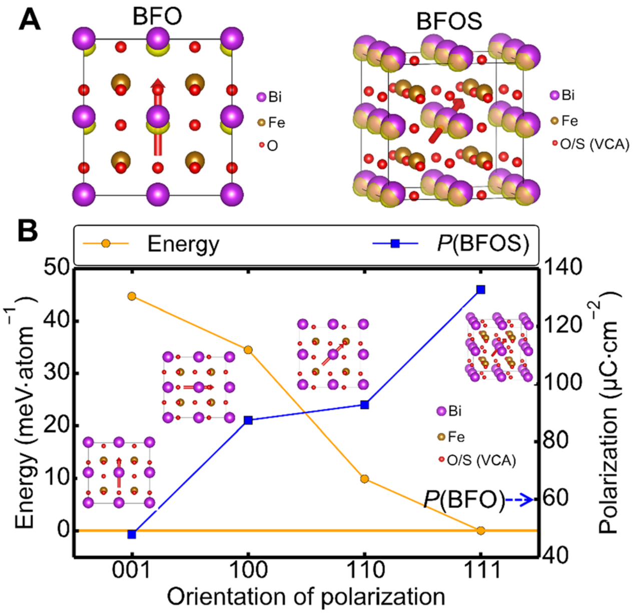

Fig. 1 Theoretical calculation of the effect on polarization vector *via* introduction of S atoms. (A) Visualization of lone-pair electron Bi sites in pristine $BiFeO_3$ (BFO) and sulfurized $BiFeO_3$ (BFOS) based on the electron localization function. (B) Total energy and ferroelectric polarization (*P*) as a function of the ferroelectric polarization orientation of BFOS.

calculations demonstrate that introducing S-atoms in BFO-based films is an effective strategy to achieve new states of matter and phenomena.

Fig. 1(B) displays the total energy and corresponding ferroelectric polarization of BFOS for different polarization directions, as well as the corresponding optimized crystal structures in the inset. In comparison to the pristine BFO model with a polarization of approximately 60.0 μC cm^{-2} (marked by the dashed arrow in Fig. 1(B)) along the [001] direction, the [111] polarization state of BFOS has the lowest energy and is most energetically favored, followed by the [110] polarization state with an energy of only 10 meV per atom higher. The ferroelectric polarizations of the [111] and [110] polarization states are 133 and 93 μC cm^{-2}, respectively. Therefore, these results suggest that introducing sulfur into BFO not only drive polarization rotation, deviating from the original [001] polarization state in pure BFO, but can also lead to a significant enhancement of the ferroelectricity.

To experimentally confirm our calculation results, a surface sulfidation[34] treatment was used for preparing BFOS thin films. First, epitaxial BFO thin films were grown on a (001)-oriented LAO substrate with an intermediate conducting (001)-oriented $SrRuO_3$ (SRO) buffer layer through radio frequency magnetron sputtering. Then, a thiourea solution was spin-coated on the surface of the prepared BFO thin films followed by pyrolysis and annealing to obtain BFOS thin films. The crystalline quality and strain of the thin films were determined by X-ray diffractometry (XRD) and synchrotron X-ray reciprocal-space mapping (RSM).[35] Fig. 2(A) confirms the epitaxial growth of BFO and BFOS along the *c*-oriented on SRO/LAO, where no second phase was observed, indicating high phase purity of the films. The (00*l*) peaks originating from the *c*-oriented epitaxial BFOS thin film showed an unexpected shift toward a larger 2θ degree, exhibiting a reduced out-of-plane lattice parameter compared to those from the BFO one. The RSM around (103) reflections of the BFO and BFOS thin films was performed to further investigate their crystal structure (Fig. 2(B)). The results confirmed that the out-of-plane lattice of BFOS achieved the expected compression under sulfurization, with a 0.5% weakening of the stress state compared to BFO. Moreover, Φ scans of the BFO and BFOS (101) planes certify that the epitaxial growth relationship was not disrupted after sulfurization (Fig. 2(C)). Direct evidence for the heteroepitaxial structures of BFO(BFOS)/SRO/LAO was provided by spherical-aberration-corrected HAADF *Z*-contrast STEM images (Fig. S1, ESI†). Moreover, the partial in-plane relaxation of the lattice parameters of BFO was also explored *via* RSM (Fig. 2(B)), revealing that the biaxial strain was released in BFO thin films. This mainly originated from the lattice mismatches of SRO (3.93 Å) and LAO (3.79 Å).[36] Therefore, we directly derived the lattice parameters of the films from the HAADF images. Fig. 2(D) and (G) clearly show both the A- and B-site cations, and their long-range ordered atomic arrangement indicates an excellent crystalline quality; the average crystal interplanar spacing of the BFO and BFOS thin films was measured through intensity profiles along *a* (Fig. 2(E) and (H)) and *c* (Fig. 2(F) and (I)) in a randomly selected area marked by orange and yellow lines, respectively. We took the average values of the *a* and *c* parameters for the strain analysis, whose results indicate that the *c*/*a* of the epitaxial films decreases from 1.048 to 1.004 after sulfurization. They also revealed the role of sulfurization in the initial structure of the BFO thin films, which introduced compressive and tensile strains along the *c* and *a* direction, respectively. A more specific description of the structural distortion is discussed below. To demonstrate the successful sulfurization of the BFO thin films, we performed STEM energy-dispersive X-ray spectroscopy (EDXS) mapping and XAS analysis to confirm the presence of S in the BFOS thin film. In the STEM-EDXS map displayed in Fig. 2(J), the S atoms are randomly distributed in the epitaxial film, indicating effective sulfurization. More importantly, the XAS spectrum of BFOS exhibited a notable S L-edge, which was not observed in BFO (Fig. 2(K)), further confirming the successful sulfurization. We obtained the content of S in the BFOS films of ∼0.58% by using STEM-EDXS (Fig. S2, ESI†). The results show that the content of S in the BFOS films is about 0.58% and the molecular formula is $BFO_{2.983}S_{0.017}$. It is known that the Goldschmidt tolerance factor (*t*) can predict stability and distortion of the crystal structure of ABO_3 perovskite materials. The *t* is defined by the expression $t = \dfrac{r_A + r_O}{\sqrt{2}(r_B + r_O)}$, where r_A, r_B, and r_O are the ionic radii of the corresponding ions. Based on the above results, the *t* of the sulfurized film is 0.8401 similar to that of the pure BFO film (0.8402), which is in the range of 0.77 to 1.11, indicating that the structure can exist stably. We have measured the XRD pattern of BFO and BFOS films at different temperatures. The temperature-dependent XRD patterns (Fig. S3, ESI†) show good thermal stability of the films.

The chemical strain engineering can induce structural distortion with the distortion of oxygen octahedra and effectively

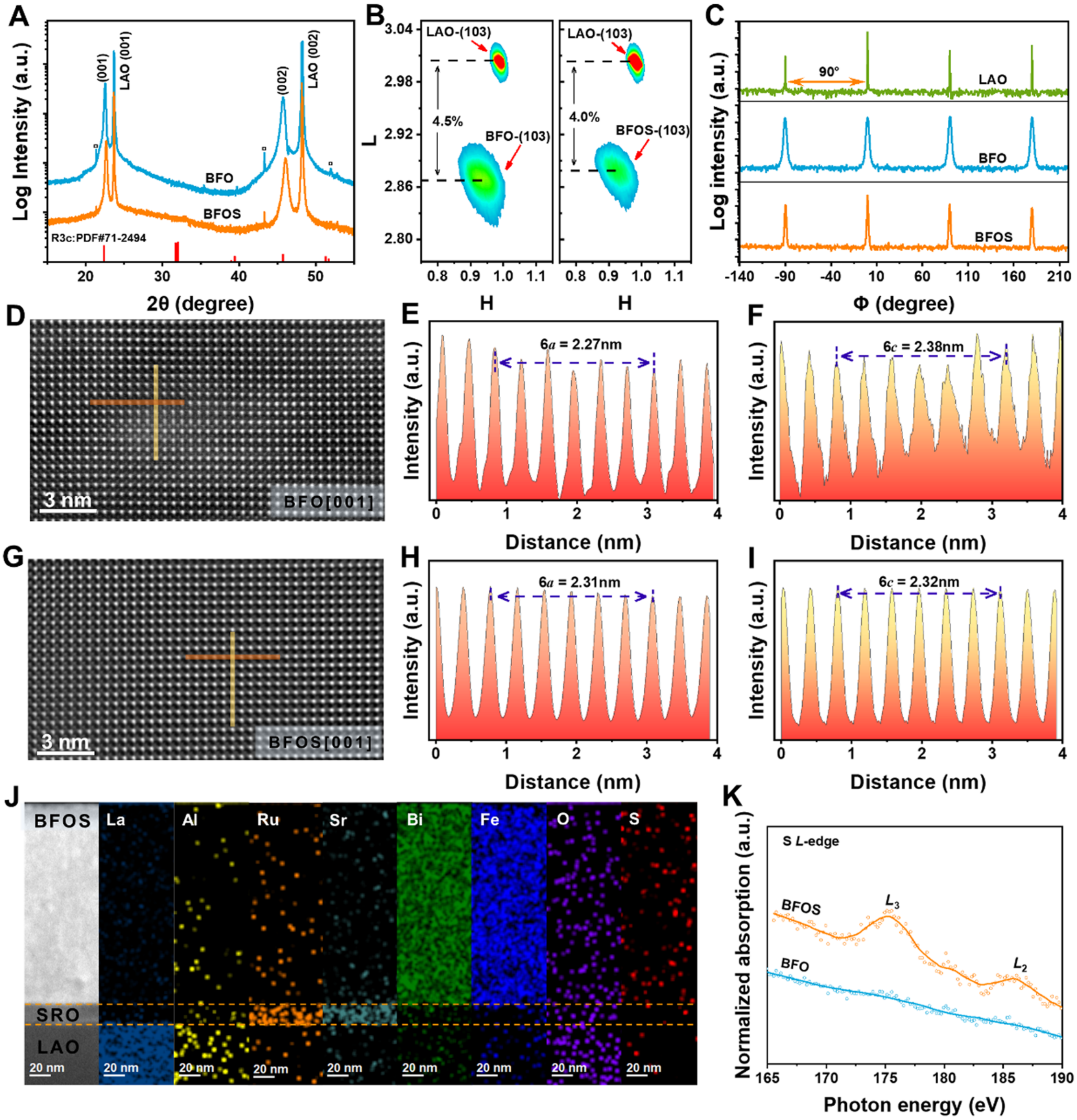

Fig. 2 Crystal structure and chemical characterization of $BiFeO_3$ (BFO) and sulfurized BFO (BFOS) thin films. (A) X-ray diffractograms and (B) synchrotron X-ray reciprocal-space mappings of BFO and BFOS. (C) Φ scans normal to the (101) plane of BFO, BFOS, and $LaAlO_3$ (LAO), respectively. (D) and (G) Atomic-scale HAADF-STEM images of BFO and BFOS thin films, six sets of interplanar spacing along (E,H) *a* and (F,I) *c* measured directly. (J) Cross-sectional scanning electron micrograph and energy-dispersive X-ray spectroscopy elemental maps of a BFOS thin film on an LAO substrate (SRO:$SrRuO_3$). (K) X-ray absorption S L-edge of BFO and BFOS.

modulate the ferroelectric polarization of BFO-based thin films. Therefore, previously unknown effects on ferroelectric properties can be expected in BFOS thin films. We measured the systematic ferroelectric polarization–electric field loops of the thin films (Fig. 3(A)), finding that the sulfurization gave a boost to P_r from 58 to 100.7 μC cm^{-2} and a substantial increase in the switching current. Note that the P_r of the two thin film types was measured at the same voltage with a positive-up negative-down (PUND) pulse sequence (Fig. S4, ESI†). The raw data ferroelectric hysteresis loops of the BFO and BFOS films are shown in Fig. S5 (ESI†). To better reflect the authenticity of these results, we analyzed the ferroelectric signals of different regions. Fig. 3(B) shows the statistical P_r distribution, with an average P_r value of 98.9 μC cm^{-2} for BFOS thin film, superior to that of the BFO one (58.3 μC cm^{-2}). By combining the experimental results with the first-principles calculations, we conjecture that the enhanced polarization may originate from the rotation of the polarization direction toward the [110] or [111] direction or a combination of the two. Then, to explore the performance of the BFO and BFOS thin films within ferroelectric device structures, we conducted retention measurements for Pt/BFO(BFOS)/SRO/LAO heterostructures (Fig. 3(C)). The retention results suggested that the ΔP [$\Delta P = P_{rt}$ (switched polarization) − P_{rn} (non-switched polarization)] of the films slightly reduced for up to 50 ms when the experiment was terminated, indicating the strong stability of the P_r against the

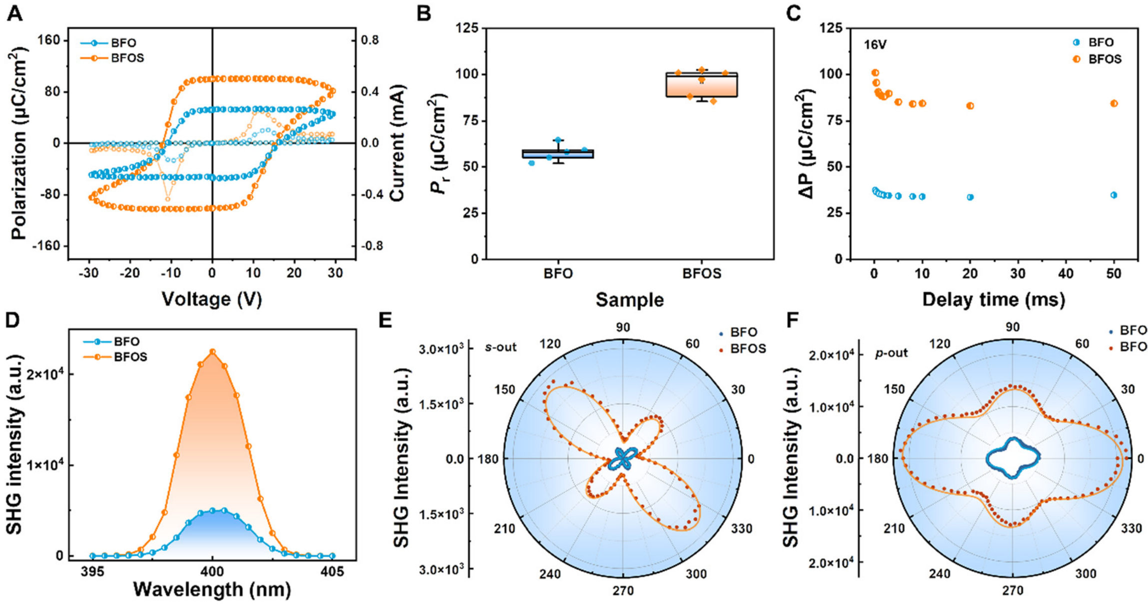

Fig. 3 Ferroelectric properties of $BiFeO_3$ (BFO) and sulfurized BFO (BFOS) thin films. (A) Positive-up negative-down measurements of BFO and BFOS at a frequency of 5 kHz. (B) Statistical remnant polarization (P_r) distribution for BFO and BFOS. (C) Retention measurements on Pt/BFO(BFOS)/$SrRuO_3$/$LaAlO_3$. (D) SHG intensity of BFO and BFOS, and their SHG patterns with the (E) s-out and (F) p-out configurations. The scattered points are experimental data, and the orange and blue lines are fitted to BFOS and BFO experimental data, respectively.

retention time. As shown in Fig. S6(A) and (B) (ESI†), the dielectric constants (ε_r) and loss tangents ($\tan\delta$) of BFO and BFOS were measured at room temperature as a function of frequency ranging from 1 kHz to 100 kHz. The dielectric constants of BFO at various frequencies are higher than those of BFOS. When the frequency increases to 10^6 Hz, the dielectric loss has an evident increase, and the dielectric constant has an obvious decrease. As shown in Fig. S6(C) (ESI†), the leakage current density of BFO is slightly lower than that of BFOS films.

Optical second-harmonic generation (SHG) was also used to semi-quantitatively characterize the polarization. In general, the media can only produce a SH signal if the spatial-inversion symmetry is broken.[37–39] In solid materials, there are two common cases in which spatial-inversion symmetry is broken, either at the surface (interface) or in the presence of ferroelectric order of the medium. BFO-based ferroelectric films, as typical ferroelectric materials, undergo local spatial-inversion symmetry breaking in their unit cells due to a displacement between the A-site ions and FeO_6 octahedra;[40] thus, the polarization P change with the film can be obtained by detecting the SH signal.[41] As depicted in Fig. 3(D)–(F), we determined the SHG intensity I_{SHG} of the BFO and BFOS thin films, as well as their polarization dependence on the incident light. Fig. 3(D) shows a violent increment in I_{SHG} after sulfurization. Considering the I_{SHG} proportional to the square of the P ($I_{SHG} \propto |P|^2$),[42,43] it reveals a ~2.12 times increase in P of sulfurized thin films and still confirms strongly the promotion of polarization enhancement of epitaxial BFO thin films by sulfurization. We also recorded the rotational anisotropy SHG patterns of the BFO and BFOS thin films (Fig. 3(E) and (F)). The s-out and p-out configurations during the measurement denote the arrangements where the analyzer polarization is vertical and parallel to the incident light field, respectively. After fitting the polarization angle dependence curves, both the s- and p-out patterns exhibited a large and a small pair of peaks, indicating that both BFO and BFOS have dual rotational symmetry. However, there was a noticeable difference in I_{SHG} between the two thin films; this further demonstrates that sulfurization induces an increase in the electric dipole moment within BFO, resulting in the enhancement of the ferroelectricity.

To obtain a better understanding of the microscopic mechanisms behind the enhanced ferroelectric properties observed in the sulfurized BFO film, an atomic-scale microstructure analysis was performed *via* spherical-aberration-corrected HAADF-STEM. Fast Fourier transform (FFT) patterns (Fig. S7, ESI†) showed that the tilt angle (β) changed from 89.8° to 90.8° after sulfurization, indicating the tendency of the thin films to shift toward the rhombohedral phase and providing evidence for a lower c/a. More significantly, we found the nuance of Fe ions in the sulfurization thin films compared to the BFO ones after detailed image inspections (Fig. 4(A) and (C)). As sulfidation proceeded, Fe ions were offset from their original positions and the distortion of the FeO_6 octahedron emerged. For a more visual representation of why the Fe ions are deflected, Fig. 4(B) and (D) schematize the following atomic structures. The original unit cell is subjected to compressive strain in the out-of-plane direction and tensile stress in the in-plane direction under sulfurization. To reach a new structural equilibrium, the Fe ions are deflected under the action of these two stresses, which increases also the relative displacement of Bi ions to the FeO_6 octahedra; this induces polarization rotation and a shift of the central charge position, enhancing the local

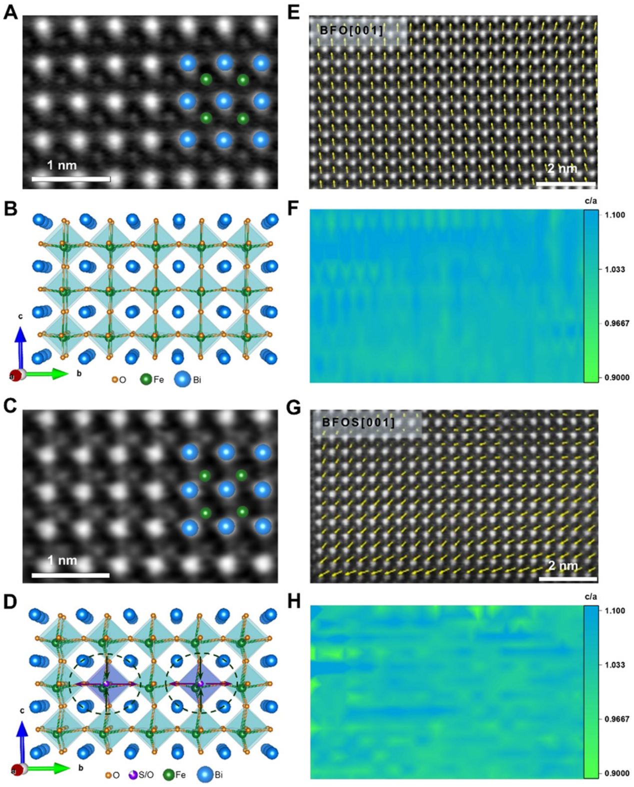

Fig. 4 Microscopic origin of robust ferroelectric properties. High-resolution transmission electron micrograph along the *a*-axis of the (A) $BiFeO_3$ (BFO) and (C) sulfurized BFO (BFOS) thin films, with the corresponding atomic schematics in (B) and (D) along the *a*-axis, where the sulfur-containing unit cells are marked by the dashed circles. (E) and (G) The polarization and (F) and (H) maps of *c*/*a* contour plots of the BFO and BFOS unit cells.

dipole moment. We determined the structural domain structure based on HAADF-STEM. We found that the domain may shift from 108° to 109° or 71° domains in the BFOS film after sulfurization by observing the polar nano-regions (Fig. S8, ESI†). Meanwhile, we can observe an increase in the coercive voltage of the BFOS film (Fig. S5, ESI†), which further confirms the change in domain structure. It is in agreement with previous reports that the 180° domain switching dominates at lower bias voltages, while 71° and 109° switching at higher voltages.[44,45] Furthermore, we plotted the polarization direction of the Fe ions and the maps of *c*/*a* contour plots of the unit cells as superimposed to a HAADF-STEM image taken along the [001] zone axis. The polarization direction within the BFO (Fig. 4(E)) and BFOS (Fig. 4(G)) thin films is marked by a yellow arrow, which directly indicates the polar distortions along the direction of [001] to the [110] and [111] under the effect of sulfurization. The results, as expected, coincide with our conjecture and the calculated trend. Through experiments and the first-principles calculations, previous studies reported an increase in the polarization values of pristine BFO as the polarization direction changes from [001] to [110] and [111].[14,20] Hence, we can deduce that the polarization rotation is likely the dominant factor causing polarization enhancement in the new sulfurized method. Moreover, the comparison in Fig. 4(F) and (H) demonstrates that the *c*/*a* of BFOS thin films tends to decrease and approach 1 under sulfurization, similar to the above results, which means that their in-plane stress is released and shifts to the possible monoclinic pseudo-cubic structure. Therefore, we can conclude that the factor causing the polarization rotation is the in-plane tensile stress caused by sulfurization.

Additional information about the lattice dynamics and interactions between the electron orbitals of the investigated films was obtained by Raman spectroscopy and XAS. If the FeO_6 octahedra produce distortion by sulfurization, the coupling between phonon and lattice symmetry in the Raman spectrum will change accordingly. As both the epitaxial BFO and BFOS thin films have a monoclinic pseudo-cubic structure and a four-axis symmetry, their structure can be expressed as $\Gamma = 3A_1 + B_1 + 4E$,[46] where the singly degenerate A_1 modes are *z*-directional while the doubly degenerate E modes are *xy*-plane polarized.[47] The peaks observed at 121.5, 138.8, 168.0, and 215.9 cm^{-1} in the Raman spectra can be assigned to the E(1TO), A_1(1TO), A_1(2TO), and A_1(3TO) modes, respectively (Fig. 5(A)). Moreover, the Bi–O bonds are associated with low-frequency modes (below 170 cm^{-1}) and the vibrating mode near 215 cm^{-1} related to FeO_6 octahedra.[48] Compared with the BFO thin film, the difference at the E(1TO) and A_1(1TO) peaks in the BFOS spectrum illustrates a sulfurization-induced change in the vibration mode of the Bi–O bonds. In particular, the lowest-frequency E(1TO) peak can be clearly observed in the BFOS spectrum, and it might have resulted from the structural distortion of the thin film toward the monoclinic pseudo-cubic structure, leading to a reduction of the A_1(1TO) mode intensity. Besides, the A_1(3TO) peak tended to move to higher frequencies after sulfurization, indicating the presence of tensile stress; this is also consistent with the shift of the Fe 2p energy level toward lower energies, while both the Bi 4f and the oxygen energy levels of the BFOS thin film shifted toward higher energies (Fig. S9, ESI†). These results confirm significant changes in the lattice dynamics due to the offset of Fe ions, which is further important evidence for the rotation of the polarization state.

Polarization distortion or rotation in oxide perovskite films is often accompanied by a change in the electronic structure.[49–51] XAS is an important tool for the characterization of the electronic structure, and studies on $PbTiO_3$,[52] $BaTiO_3$,[53] $SmFeO_3$,[54] *etc.* have demonstrated its important role in the analysis of polarity changes. Therefore, the origin of the enhanced ferroelectric properties in BFOS thin films with polarization distortion relative to the initial BFO can also be traced using XAS. According to the crystal field theory, in an ideal FeO_6 octahedron with a cubic structure, the 5-times-degenerate 3d orbitals of Fe atoms split into doublet e_g and triplet t_{2g} levels (Fig. 5(B)). For BFO thin films with a pseudo-cubic structure, the degenerate orbitals further split due to the Jahn–Teller effect,[55] the doublet e_g further splits into $d_{x^2-y^2}$ and $d_{3z^2-r^2}$, and the triplet t_{2g} splits into d_{xy}, d_{xz}, and d_{zx}. Based on the above discussion, the compressive and tensile strains are introduced along the out-of-plane and in-plane directions, respectively, due to the sulfurization. Moreover, the Fe ions shift along the [110] or [111] direction with distortion of the FeO_6 octahedra, resulting in the rotation of the polarization. Therefore, the Fe coordination environments in BFO and BFOS thin films will

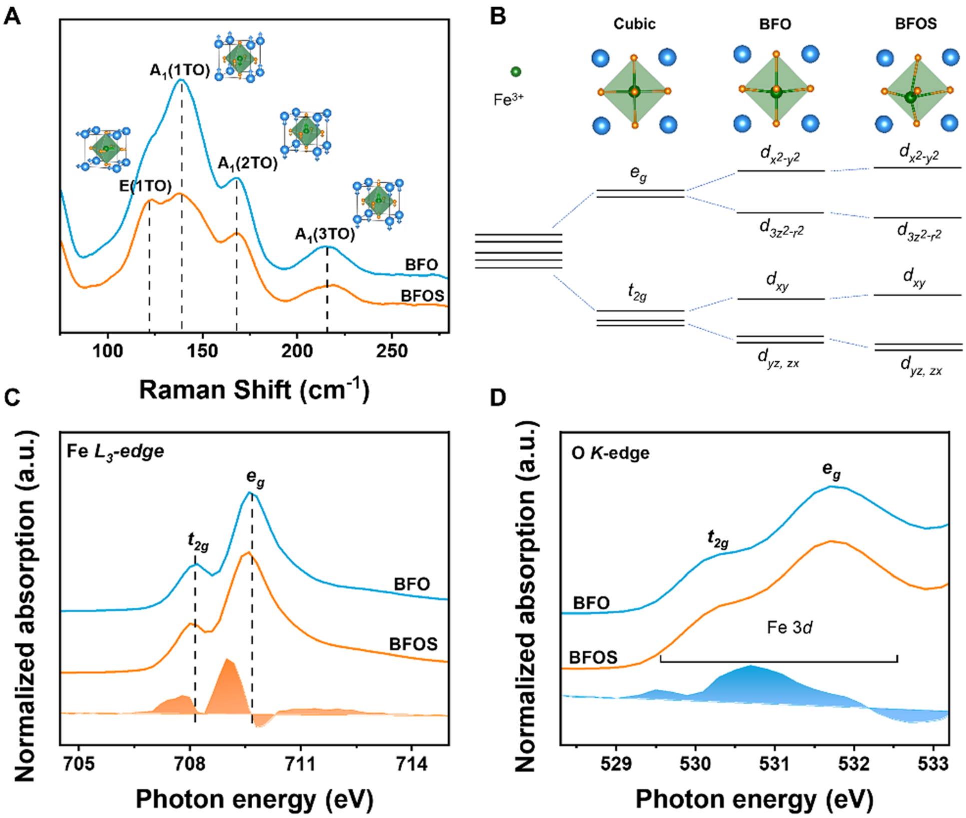

Fig. 5 Lattice dynamics and electronic structure analysis. (A) Raman spectra of $BiFeO_3$ (BFO) and sulfurized BFO (BFOS), along with schematics of zone-center vibrational normal modes for the tetragonal BFO with *P4mm* symmetry (insets). (B) Schematic of the 3d orbital of Fe in the FeO_6 octahedron. (C) X-ray absorption Fe L_3-edge and (D) O K-edge spectra of BFO and BFOS; the blue- and orange-outlined areas indicate the difference obtained by subtracting the intensity of BFO from that of BFOS.

change, as explored by the XAS O K-edge and Fe L-edge spectra. In general, the splitting of both e_g and t_{2g} should decrease with the reduced *c*/*a*. However, the difference in energy by subtracting the intensity of BFO from that of BFOS increases at first, then decreases, and increases at last, suggesting an increasing split of t_{2g} (e_g) for the BFOS films (Fig. 5(C)). This subsequently proves that the BFO thin films transform into a monoclinic pseudo-cubic structure with small *c*/*a* ratio under sulfidation, resulting in increased lattice distortion. Moreover, Fe–O/S bonds (the O/S atoms along the *ab*-plane of the octahedron) increase because of the polarization rotation toward the [110] or [111] direction, weakening the coupling between Fe 3d $d_{3z^2-r^2}$ (d_{xz} and d_{zx}) and O 2p. Fig. 5(D) displays a similar trend for the XAS Fe L-edge spectra. More importantly, it has also been supported by the weakening of the Fe 2p energy level (Fig. S9, ESI†). Therefore, the main reason for the observed ferroelectric enhancement lies in the polarity distortion caused by the polarization rotation under the effect of sulfurization in BFOS thin films.

Conclusion

In summary, we successfully prepared epitaxial S-substituted BFO thin films through a feasible approach. We got direct evidence of largely enhanced ferroelectricity in the sulfurized films, which has been supported by both theoretical calculations and experiments. This study suggests that the polarization enhancement is caused by the sulfurization-driven polarization rotation. Our work highlights the enormous potential of utilizing anion-induced polarization state changes in diverse oxide materials, paving the way for a new generation of multifunctional materials with exceptional performance.

Data and materials availability

All data needed to evaluate the conclusions in the paper are present in the paper and/or the ESI.†

Author contributions

L. Z., G. X., and Z. P., conceived the idea of the work. G. X. and J.D., fabricated the thin films. Y.-W. F. performed the theoretical calculations. G. X., J. T., and Q. Y., conducted the XRD, RSM, and XAS characterizations. G. X. H. L., and J. D., carried out the ferroelectric property measurements. K. J., Y. L., and S. X. performed the SHG experiments. X. Z., D. Z., Q. W., and C. L. performed the STEM measurements. L. Z., Z. P., Y.-W. F., S. D., H. L., and S. X. contributed to the data analysis and interpretation.

G. X., L. Z., Z. P., and Y.-W. F. wrote the manuscript with contributions from others.

Conflicts of interest

The authors declare that they have no competing interests.

Acknowledgements

This work was supported by the National Key Research and Development Program of China (2018YFA0703700, 2017YFE0119700, 2021YFA1400300 and 2018YFA0305700), the National Natural Science Foundation of China (21801013, 51774034, 22271309, 11721404, 11934017, 12261131499, and 51961135107), the Fundamental Research Funds for the Central Universities (FRF-IDRY-19-007 and FRF-TP-19-055A2Z), the National Program for Support of Top-notch Young Professionals, the Young Elite Scientists Sponsorship Program by CAST (2019-2021QNRC), the Beijing Natural Science Foundation (Z200007), and the Chinese Academy of Sciences (XDB33000000). This research used the resources of the Beijing Synchrotron Radiation Facility (1W1A and 4B9B beamlines) of the Chinese Academy of Science. We thank H.H. Wang and Y. Chen for the measurement of RSM, and C. Liu and K. Q. Nie for the measurement of XAS.

References

1 X.-K. Wei, C.-L. Jia, H.-C. Du, K. Roleder, J. Mayer and R. E. Dunin-Borkowski, *Adv. Mater.*, 2020, **32**, 1907208.
2 Z. Pan, M.-H. Zhang, T. Nishikubo, Y. Sakai, H. Yamamoto, H. Hojo, M. Fukuda, L. Hu, H. Ishizaki, S. Kaneko, S. Kawaguchi, J. Koruza, J. Rödel and M. Azuma, *ACS Appl. Mater. Interfaces*, 2021, **13**, 5208–5215.
3 L. Yang, H. Huang, Z. Xi, L. Zheng, S. Xu, G. Tian, Y. Zhai, F. Guo, L. Kong, Y. Wang, W. Lü, L. Yuan, M. Zhao, H. Zheng and G. Liu, *Nat. Commun.*, 2022, **13**, 2444.
4 Z. Tan, J. Xing, Y. Peng, Q. Zhang and J. Zhu, *Phys. Rev. B*, 2021, **104**, 014104.
5 V. Petkov, J.-W. Kim, S. Shastri, S. Gupta and S. Priya, *Phys. Rev. B: Condens. Matter Mater. Phys.*, 2020, **4**, 014405.
6 D. Kan, V. Anbusathaiah and I. Takeuchi, *Adv. Mater.*, 2011, **23**, 1765–1769.
7 X. Dong, X. Li, H. Chen, Q. Dong, J. Wang, X. Wang, Y. Pan, X. Chen and H. Zhou, *J. Adv. Ceram.*, 2022, **11**, 729–741.
8 T. Choi, S. Lee, Y. J. Choi, V. Kiryukhin and S. W. Cheong, *Science*, 2009, **324**, 63–66.
9 F. Pailloux, M. Couillard, S. Fusil, F. Bruno, W. Saidi, V. Garcia, C. Carrétéro, E. Jacquet, M. Bibes, A. Barthélémy, G. A. Botton and J. Pacaud, *Phys. Rev. B: Condens. Matter Mater. Phys.*, 2014, **89**, 104106.
10 J. K. Shenton, D. R. Bowler and W. L. Cheah, *Phys. Rev. B*, 2019, **100**, 085120.
11 D. Ji, S. Cai, T. R. Paudel, H. Sun, C. Zhang, L. Han, Y. Wei, Y. Zang, M. Gu, Y. Zhang, W. Gao, H. Huyan, W. Guo, D. Wu, Z. Gu, E. Y. Tsymbal, P. Wang, Y. Nie and X. Pan, *Nature*, 2019, **570**, 87–90.
12 Y. Zhang, C. Ma, X. Lu and M. Liu, *Mater. Horiz.*, 2019, **6**, 911–930.
13 N. Wang, X. Luo, L. Han, Z. Zhang, R. Zhang, H. Olin and Y. Yang, *Nano-Micro Lett.*, 2020, **12**, 81.
14 J. B. Neaton, C. Ederer, U. V. Waghmare, N. A. Spaldin and K. M. Rabe, *Phys. Rev. B: Condens. Matter Mater. Phys.*, 2005, **71**, 014113.
15 L. W. Martin and A. M. Rappe, *Nat. Rev. Mater.*, 2016, **2**, 16087.
16 A. R. Damodaran, J. C. Agar, S. Pandya, Z. Chen, L. Dedon, R. Xu, B. Apgar, S. Saremi and L. W. Martin, *J. Phys.: Condens. Matter*, 2016, **28**, 263001.
17 J. Wang, J. B. Neaton, H. Zheng, V. Nagarajan, S. B. Ogale, B. Liu, D. Viehland, V. Vaithyanathan, D. G. Schlom, U. V. Waghmare, N. A. Spaldin, K. M. Rabe, M. Wuttig and R. Ramesh, *Science*, 2003, **299**, 1719–1722.
18 J. X. Zhang, Q. He, M. Trassin, W. Luo, D. Yi, M. D. Rossell, P. Yu, L. You, C. H. Wang, C. Y. Kuo, J. T. Heron, Z. Hu, R. J. Zeches, H. J. Lin, A. Tanaka, C. T. Chen, L. H. Tjeng, Y. H. Chu and R. Ramesh, *Phys. Rev. Lett.*, 2011, **107**, 147602.
19 R. R. Das, D. M. Kim, S. H. Baek, C. B. Eom, F. Zavaliche, S. Y. Yang, R. Ramesh, Y. B. Chen, X. Q. Pan, X. Ke, M. S. Rzchowski and S. K. Streiffer, *Appl. Phys. Lett.*, 2006, **88**, 242904.
20 J. Li, J. Wang, M. Wuttig, R. Ramesh, N. Wang, B. Ruette, A. P. Pyatakov, A. K. Zvezdin and D. Viehland, *Appl. Phys. Lett.*, 2004, **84**, 5261–5263.
21 S.-E. Park and T. R. Shrout, *J. Appl. Phys.*, 1997, **82**, 1804–1811.
22 D. Kan, L. Pálová, V. Anbusathaiah, C. J. Cheng, S. Fujino, V. Nagarajan, K. M. Rabe and I. Takeuchi, *Adv. Funct. Mater.*, 2010, **20**, 1108–1115.
23 K. Shimizu, H. Hojo, Y. Ikuhara and M. Azuma, *Adv. Mater.*, 2016, **28**, 8639–8644.
24 L. Bian, J.-b Xu, M.-x Song, H.-l Dong and F.-q Dong, *RSC Adv.*, 2013, **3**, 25129–25135.
25 J. Wang, H. Li, H. Li, S. Yin and T. Sato, *Solid State Sci.*, 2009, **11**, 182–188.
26 F.-F. Li, D.-R. Liu, G.-M. Gao, B. Xue and Y.-S. Jiang, *Appl. Catal., B*, 2015, **166–167**, 104–111.
27 G. Amarsanaa, D. Odkhuu, C. Won Ahn and I. W. Kim, *J. Appl. Phys.*, 2014, **116**, 194105.
28 J. A. Brehm, H. Takenaka, C.-W. Lee, I. Grinberg, J. W. Bennett, M. R. Schoenberg and A. M. Rappe, *Phys. Rev. B: Condens. Matter Mater. Phys.*, 2014, **89**, 195202.
29 L. Wei, C. Li, J. Guo, L. Guan, Y. Wang and B. Liu, *Phys. Chem. Chem. Phys.*, 2020, **22**, 11382–11391.
30 Y.-W. Fang and H. Chen, *Commun. Mater.*, 2020, **1**, 1.
31 Y. Shen, J. Cai, H.-C. Ding, X.-W. Shen, Y.-W. Fang, W.-Y. Tong, X.-G. Wan, Q. Zhao and C.-G. Duan, *Adv. Theory Simul.*, 2019, **2**, 1900029.
32 Y.-W. Fang, C. A. J. Fisher, A. Kuwabara, X.-W. Shen, T. Ogawa, H. Moriwake, R. Huang and C.-G. Duan, *Phys. Rev. B*, 2017, **95**, 014111.
33 L. Bellaiche and D. Vanderbilt, *Phys. Rev. B: Condens. Matter Mater. Phys.*, 2000, **61**, 7877–7882.

34 X. D. Li, W. X. Zhang, X. M. Guo, C. Y. Lu, J. Y. Wei and J. F. Fang, *Science*, 2022, **375**, 434–437.

35 T.-Y. Yang, W. Wen, G.-Z. Yin, X.-L. Li, M. Gao, Y.-L. Gu, L. Li, Y. Liu, H. Lin, X.-M. Zhang, B. Zhao, T.-K. Liu, Y.-G. Yang, Z. Li, X.-T. Zhou and X.-Y. Gao, *Nucl. Sci. Tech.*, 2015, **26**, 020101.

36 C. B. Eom, R. J. Cava, R. M. Fleming, J. M. Phillips, R. B. vanDover, J. H. Marshall, J. W. P. Hsu, J. J. Krajewski and W. F. Peck, *Science*, 1992, **258**, 1766–1769.

37 G. De Luca, P. Schoenherr, J. Mendil, D. Meier, M. Fiebig and M. Trassin, *Phys. Rev. Appl.*, 2018, **10**, 054030.

38 M. Trassin, G. D. Luca, S. Manz and M. Fiebig, *Adv. Mater.*, 2015, **27**, 4871–4876.

39 T. Hoffmann, P. Thielen, P. Becker, L. Bohatý and M. Fiebig, *Phys. Rev. B: Condens. Matter Mater. Phys.*, 2011, **84**, 184404.

40 R. J. Zeches, M. D. Rossell, J. X. Zhang, A. J. Hatt, Q. He, C. H. Yang, A. Kumar, C. H. Wang, A. Melville, C. Adamo, G. Sheng, Y. H. Chu, J. F. Ihlefeld, R. Erni, C. Ederer, V. Gopalan, L. Q. Chen, D. G. Schlom, N. A. Spaldin, L. W. Martin and R. Ramesh, *Science*, 2009, **326**, 977–980.

41 S. A. Denev, T. T. A. Lummen, E. Barnes, A. Kumar and V. Gopalan, *J. Am. Ceram. Soc.*, 2011, **94**, 2699–2727.

42 H. Pan, S. Lan, S. Xu, Q. Zhang, H. Yao, Y. Liu, F. Meng, E.-J. Guo, L. Gu, D. Yi, X. R. Wang, H. Huang, J. L. MacManus-Driscoll, L.-Q. Chen, K.-J. Jin, C.-W. Nan and Y.-H. Lin, *Science*, 2021, **374**, 100–104.

43 M. Müller, Y.-L. Huang, S. Vélez, R. Ramesh, M. Fiebig and M. Trassin, *Adv. Mater.*, 2021, **33**, 2104688.

44 Y. Liu, Y. Wang, J. Ma, S. Li, H. Pan, C.-W. Nan and Y.-H. Lin, *Prog. Mater. Sci.*, 2022, **127**, 100943.

45 F. Zavaliche, P. Shafer, R. Ramesh, M. P. Cruz, R. R. Das, D. M. Kim and C. B. Eom, *Appl. Phys. Lett.*, 2005, **87**, 252902.

46 M. K. Singh, S. Ryu and H. M. Jang, *Phys. Rev. B: Condens. Matter Mater. Phys.*, 2005, **72**, 132101.

47 P. Chen, X. Xu, C. Koenigsmann, A. C. Santulli, S. S. Wong and J. L. Musfeldt, *Nano Lett.*, 2010, **10**, 4526–4532.

48 T. Wang, T. Xu, S. Gao and S. H. Song, *Ceram. Int.*, 2017, **43**, 4489–4495.

49 T. Jia, H. Wu, G. Zhang, X. Zhang, Y. Guo, Z. Zeng and H.-Q. Lin, *Phys. Rev. B: Condens. Matter Mater. Phys.*, 2011, **83**, 174433.

50 R. E. Cohen, *Nature*, 1992, **358**, 136–138.

51 T. Junghoefer, A. Calzolari, I. Baev, M. Glaser, F. Ciccullo, E. Giangrisostomi, R. Ovsyannikov, F. Kielgast, M. Nissen, J. Schwarz, N. M. Gallagher, A. Rajca, M. Martins and M. B. Casu, *Chem*, 2022, **8**, 801–814.

52 L. Zhang, J. Chen, L. Fan, O. Dieguez, J. Cao, Z. Pan, Y. Wang, J. Wang, M. Kim, S. Deng, J. Wang, H. Wang, J. Deng, R. Yu, J. F. Scott and X. Xing, *Science*, 2018, **361**, 494–497.

53 Y. Wang, L. Zhang, J. Wang, Q. Li, H. Wang, L. Gu, J. Chen, J. Deng, K. Lin, L. Huang and X. Xing, *J. Am. Chem. Soc.*, 2021, **143**, 6491–6497.

54 H. Li, Y. Yang, S. Deng, L. Zhang, S. Cheng, E.-J. Guo, T. Zhu, H. Wang, J. Wang, M. Wu, P. Gao, H. Xiang, X. Xing and J. Chen, *Sci. Adv.*, 2022, **8**, eabm8550.

55 K.-T. Ko, M. H. Jung, Q. He, J. H. Lee, C. S. Woo, K. Chu, J. Seidel, B.-G. Jeon, Y. S. Oh, K. H. Kim, W.-I. Liang, H.-J. Chen, Y.-H. Chu, Y. H. Jeong, R. Ramesh, J.-H. Park and C.-H. Yang, *Nat. Commun.*, 2011, **2**, 567.